Energy Transport and Dissipation in DIII-D Detached Divertor Plasmas

A.W. Leonard[1], A.E. Jaervinen[2], S.L. Allen[2], A.G. McLean[2], C.M. Samuell[2]

[1]General Atomics, San Diego, USA
[2]Lawrence Livermore National Laboratory, Livermore, USA

Introduction: Highly dissipative, or detached, divertor plasma operation will be a critical feature of future tokamaks in order to not exceed material limits of the divertor target. Models to describe and predict divertor dissipation encompass a range of complexity from analytic models [1] used to explore scaling trends to 2D computational models [2] for detailed specific divertor configurations. In order to test these models and develop understanding of the underlying physics processes controlling boundary heat flux dissipation, a series of highly dissipative divertor plasmas in DIII-D were examined with a comprehensive diagnostic set.

Detached divertor conditions in DIII-D were obtained in an open Lower-Single-Null (LSN) configuration with ~ 3MW of heating to produce H-mode plasmas with ELMs at frequency of ~ 25 Hz. The plasma current of 1.3 MA and toroidal field of 2.0 T resulted in q_{95} ~3.3. D_2 gas injection, ~80 torr-l/s, produced detached divertor conditions with $T_{e,div} \leq 5$ eV. Approximately 2/3 of the energy dissipation was due to intrinsic carbon impurity radiation as measured by VUV spectroscopy [3]. The divertor plasma was swept across the view locations of a Divertor Thomson Scattering system (DTS) for 2D profiles of divertor T_e and n_e. [4] Data was collected later in the ELM phase when SOL and divertor conditions came into equilibrium, ~ 5 ms after the ELM pulse. For power balance the divertor radiation 2D profile is inverted from two 24-channel bolometer arrays.

In the following analysis detached divertor conditions will be found to dissipate essentially all of the core plasma heat exhaust. Modeling with the 2D fluid code UEDGE reproduces these results and indicates that the divertor plasma conditions (n_e, T_e) required to achieve this dissipation are determined by convective transport, with poloidal ExB flow providing a large part of this transport.

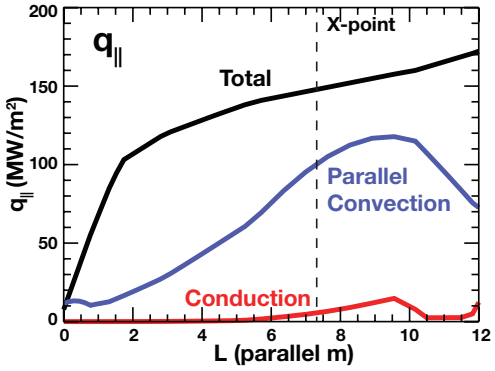

Figure 1: Total parallel heat flux (black) in the outboard divertor from power balance. Also shown are heat fluxes from conduction (red) inferred from the T_e profile and the convected heat flux for sonic flow towards the target.

Experimental Measurements of Divertor Energy Transport and Dissipation: Previous analysis in DIII-D has found that convection must be invoked to describe heat transport reconstructed from power balance in the divertor

[5,6]. The 2D radiation profile from bolometery is integrated from the target heat flux upstream as a function of parallel distance, $\partial q_{\parallel}/\partial s = S$, where s is the parallel distance and S is the radiated power density. As the radial resolution of the bolometer arrays is insufficient, the width of the heat flux channel is assumed to be that measured upstream by Thomson scattering, $\lambda_q \sim 2/7\,\lambda_{Te}$, consistent with the ITPA heat flux width scaling [7] and DTS measurements of the divertor plasma. The very low heat flux carried to the target by the plasma is confirmed with target Langmuir probes, the lowest channel of DTS and an IR camera heat flux that can be accounted for largely by radiative heating of the surface. As shown in Fig. 1, ~ 150 MW/m^2 of heat flux flows into the divertor, with essentially all of this power, ≥95%, radiated away before striking the divertor target.

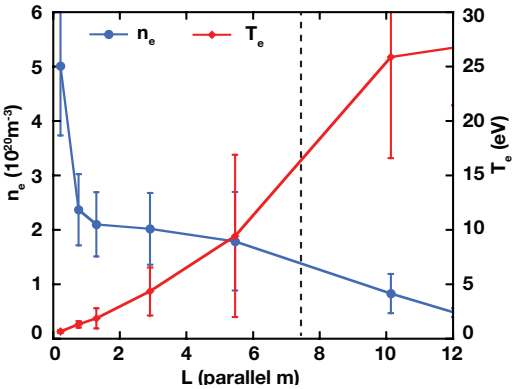

Figure 2; Profile of n_e and T_e within the heat flux channel, as a function of parallel distance from the divertor target

T_e and n_e from DTS are used to identify transport channels carrying heat flux from the divertor entrance towards the target. Profiles of n_e and T_e as a function of parallel distance from the target shown in Fig. 2 are obtained by selecting DTS data within λ_q of the separatrix in the latter half of the ELM phase during constant detached conditions. In this detached state T_e is low, ≤ 10 eV through the bulk of the divertor plasma, decreasing to ≤ 1eV at the target. n_e is high, ≥ 2x10^{20} m^{-2}, and increasing towards the target. The low and flat T_e profile implies very little of the parallel heat flux is carried by electron thermal conduction, $q_{cond} = \kappa T_e^{5/2}\,\partial T_e/\partial s$, as shown in Fig. 1. Coherence Imaging Spectroscopy (CIS) of CIII visible emission indicates near sonic parallel plasma flow towards the divertor target [8]. The contribution of sonic plasma flow to parallel energy transport, $q_{conv} = nv_{\parallel}\{5/2\,(T_e + T_i) + 1/2\,mv_{\parallel}^2 + I_0\}$ is evaluated from the profiles of Fig. 2 and shown in Fig. 1. T_i is assumed equal to T_e at these collisionalities. While the contribution of sonic parallel flow to heat flux is significant in the divertor, it can only account for ~ 1/3 of the observed energy transport.

Modeling with UEDGE: The discharges described above were modeled with the 2D multi-fluid code UEDGE, utilizing full plasma drifts to examine their role in divertor transport [2]. Radial transport coefficients were adjusted to match the upstream experimental profiles, resulting in a SOL heat flux width consistent with ITPA scaling. Radial power flow through the inner boundary was set to match power balance, resulting in a parallel heat flux flowing into the divertor similar to experiment as shown in Fig. 1. The recycled deuterium is modeled

as a neutral fluid with unity recycling at the target and R=0.99 at the radial boundaries in the SOL and private flux region (PFR). The overall density is set by specifying the density at the inner core boundary. This results in a modest radial ion flux at the inner boundary to make up for the ions lost at the outer boundary.

The resulting modeled n_e and T_e profiles along a flux tube just outside of the separatrix from the divertor entrance to the target are shown in Fig. 3. While the modeled T_e is slightly higher (25 eV vs. 17 eV) than experiment at the divertor entrance, both continuously decrease to $\leq$ 1 eV at the target. The modeling does not achieve as high a density at the target, but they both exhibit similar densities, 1-2x10^{20} m^{-3} through much of the divertor. The modeled energy transport, Fig. 4, is similar to that inferred from experiment, with ~150 MW/m^2 flowing into the divertor with near complete (95%) dissipation before striking the divertor target. With a larger T_e gradient the modeled conductive heat flux is higher than inferred from experiment, but still a small fraction of the total heat flux. Parallel convection contributes a larger fraction of the heat flux, but also remains less than half the total similar to experiment. The poloidal E×B heat flux plotted in Fig. 4 is projected into the parallel direction for an "effective" parallel flux for comparison with the other parallel fluxes.

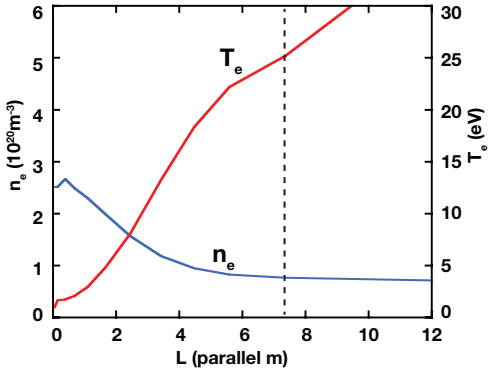

Figure 3; UEDGE simulation of n_e and T_e as a function of the parallel distance from the divertor target for the poloidal flux tube just outboard of the separatrix.

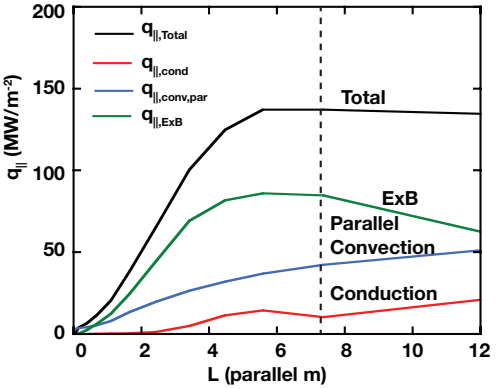

Figure 4; UEDGE simulation of parallel heat flux. Shown are total heat flux (black), and that due to conduction (red), parallel convection (blue), and "effective" parallel heat flux due to poloidal ExB plasma flow (green).

The convective transport shown in Fig. 4 must be consistent with overall particle transport into and out of the divertor. Plotted in Fig. 5 are radial profiles of ion flux at the divertor entrance, just below the X-point from the PFR to the outer SOL boundaries in the UEDGE simulation. The "effective" parallel ion flux flows towards the target with poloidal E×B flow is greatest in the near SOL with parallel ion flow dominant in the far SOL. In the PFR E×B flow carries significant ion flux out of the divertor. Integrating the entire radial profile indicates a total of 3.0×10^{22} particles flowing into the outer divertor. This implies ~50% of the outboard divertor neutral source due to recycling and recombination escapes the divertor.

Discussion: In DIII-D detached divertor plasmas both experiment and modeling imply plasma convection can dominate energy transport through the bulk of the divertor volume, even

in regions with $T_e \geq 20$ eV. The implication of convective transport is reduced T_e gradients which provide greater volume of plasma for efficient impurity radiation, $T_e < 20$ eV, and ultimately plasma recombination, $T_e \leq 1$ eV. Both experiment and modeling exhibit near complete dissipation of the heat flux carried by the plasma before arrival at the target. Both data and simulation are consistent with both parallel and ExB poloidal flow contributing significantly to the convective transport. The open divertor DIII-D divertor configuration allows for the large overall convection as implied by the large neutral escape fraction seen in the modeling. In more closed divertors with better neutral trapping, the convective transport might be expected to be less. However, particles can still escape closed divertors with E×B flow through the PFR, driving additional flow towards the target in the common flux region. Such drift effects in a closed divertor have recently been documented in the new small angle slot divertor in DIII-D [9]. In addition, divertor target shaping may modify the ionization profile in the divertor resulting in 2D flow patterns even for little neutral escape. This work highlights the importance of particle balance resulting from both parallel and E×B flows in understanding and predicting divertor heat flux dissipation.

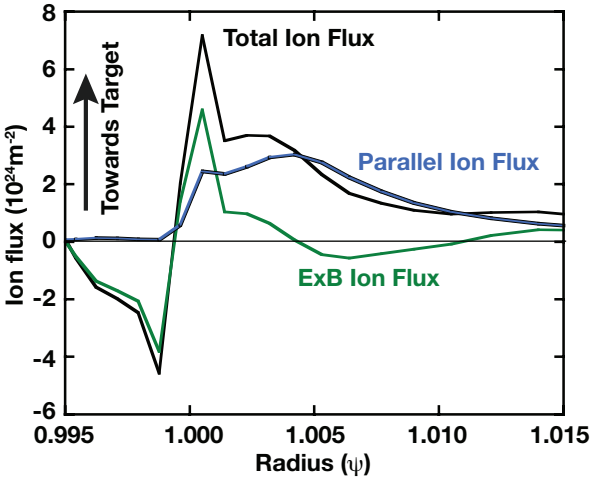

Figure 5; Ion flux into the divertor entrance with total parallel flux (black), parallel flow (blue) and poloidal ExB "effective" parallel flux.

This work has been supported by the U.S. DOE under the Contracts No.DE-FC02-04ER54698.

References

[1] M.L. Reinke, 2017 Nucl. Fusion **57** 034004

[2] A.E. Jaervinen, submitted to Nucl. Fusion

[3] A.G. McLean, et. al., submitted to Phys. Plasmas

[4] A.G. McLean, *et. al.*, 2015 Jour. Nucl. Mater. **463** 533

[5] A.W. Leonard, *et. al.*, 1997 Phys. Rev. Lett. **78** 4769

[6] A.W. Leonard, *et. al.*, 2012 Nucl. Fusion **52** 063015

[7] T. Eich, *et. al.*, 2013 Nucl. Fusion **53** 093031

[8] C.M. Samuell *et. al.*, 2018 Phys Plasmas **25** 056110

[9] Guo et al 2019 *Nucl. Fusion* https://doi.org/10.1088/1741-4326/ab26ee